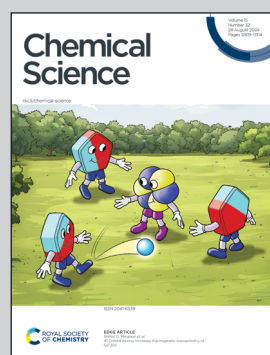


Showcasing the collaborative research coordinated by the Institute of Nanotechnology within the Cluster of Excellence “3D Matter Made to Order” at the Karlsruhe Institute of Technology, Germany.

Two- and three-photon processes during photopolymerization in 3D laser printing

The performance of a photoinitiator is key to control efficiency and resolution in 3D laser nanoprinting. Upon light absorption, a cascade of competing photophysical processes leads to photochemical reactions toward radical formation that initiates free radical polymerization. This study explores the mechanisms of photoactivation and radical formation during 3D laser printing using photoresists with a DETC photoinitiator. The role of DETC in high triplet states during radical polymerization is revealed.

### As featured in:



See Mariana Kozlowska *et al.*, *Chem. Sci.*, 2024, **15**, 12695.



Cite this: *Chem. Sci.*, 2024, **15**, 12695

All publication charges for this article have been paid for by the Royal Society of Chemistry

## Two- and three-photon processes during photopolymerization in 3D laser printing†

Anna Mauri, <sup>a</sup> Pascal Kiefer, <sup>b</sup> Philipp Neidinger, <sup>cd</sup> Tobias Messer, <sup>b</sup> N. Maximilian Bojanowski, <sup>†a</sup> Liang Yang, <sup>ab</sup> Sarah Walden, <sup>d</sup> Andreas-Neil Unterreiner, <sup>c</sup> Christopher Barner-Kowollik, <sup>ad</sup> Martin Wegener, <sup>ab</sup> Wolfgang Wenzel <sup>a</sup> and Mariana Kozlowska <sup>\*a</sup>

The performance of a photoinitiator is key to control efficiency and resolution in 3D laser nanoprinting. Upon light absorption, a cascade of competing photophysical processes leads to photochemical reactions toward radical formation that initiates free radical polymerization (FRP). Here, we investigate 7-diethylamino-3-thenoylcoumarin (DETC), belonging to an efficient and frequently used class of photoinitiators in 3D laser printing, and explain the molecular bases of FRP initiation upon DETC photoactivation. Depending on the presence of a co-initiator, DETC causes radical generation either upon two-photon- or three-photon excitation, but the mechanism for these processes is not well understood so far. Here, we show that the unique three-photon based radical formation by DETC, in the absence of a co-initiator, results from its excitation to highly excited triplet states. They allow a hydrogen-atom transfer reaction from the pentaerythritol triacrylate (PETA) monomer to DETC, enabling the formation of the reactive PETA alkyl radical, which initiates FRP. The formation of active DETC radicals is demonstrated to be less spontaneous. In contrast, photoinitiation in the presence of an onium salt co-initiator proceeds *via* intermolecular electron transfer after the photosensitization of the photoinitiator to the lowest triplet excited state. Our quantum mechanical calculations demonstrate photophysical processes upon the multiphoton activation of DETC and explain different reactions for the radical formation upon DETC photoactivation. This investigation for the first time describes possible pathways of FRP initiation in 3D laser nanoprinting and permits further rational design of efficient photoinitiators to increase the speed and sensitivity of 3D laser nanoprinting.

Received 29th May 2024  
Accepted 12th July 2024

DOI: 10.1039/d4sc03527e  
[rsc.li/chemical-science](http://rsc.li/chemical-science)

## Introduction

3D laser nanolithography is intensely investigated<sup>1,2</sup> to enable manufacturing of devices with increasing speed and resolution.<sup>2,3</sup> The strong three-dimensional spatial confinement of the exposed region in two-photon polymerization (TPP) enables resolutions that cannot be achieved using traditional one-step one-photon absorption (1PA) processes.<sup>2,4,5</sup> Despite the

tremendous progress in recent years,<sup>6</sup> 3D laser nanoprinting using TPP still faces different limitations<sup>7–10</sup> in resolution and speed that correlates strongly with the threshold laser power. This, in part, results from the limitations of the available photoinitiators (PIs) and resins: Kiefer *et al.*<sup>11</sup> have reported a strong dependence of the printing sensitivity on the TPP initiation and, therefore, on the photochemical properties of the photoinitiator. Unfortunately, the photoinduced properties of common PIs cannot be deduced straightforwardly from their chemical composition and the electronic structure in the ground state or the lowest triplet state. Moreover, despite significant progress in 3D laser nanoprinting and the design of new two-photon PIs,<sup>12–16</sup> a deep understanding of the photophysical and photochemical processes occurring upon multiphoton absorption is still scarce.<sup>17,18</sup> Molecular-based structure–activity relationships for the dependencies observed experimentally, as well as the virtual design of new PIs towards higher 3D laser nanoprinting sensitivity should be improved.

Multiphoton photoinitiation involves complex photophysical processes between the excited states of the photoinitiator that goes beyond the conventional studies of the

<sup>a</sup>Institute of Nanotechnology (INT), Karlsruhe Institute of Technology (KIT), Kaiserstraße 12, 76131 Karlsruhe, Germany. E-mail: mariana.kozlowska@kit.edu

<sup>b</sup>Institute of Applied Physics (APH), Karlsruhe Institute of Technology (KIT), Kaiserstraße 12, 76131 Karlsruhe, Germany

<sup>c</sup>Institute of Physical Chemistry (IPC), Karlsruhe Institute of Technology (KIT), Kaiserstraße 12, 76131 Karlsruhe, Germany

<sup>d</sup>School of Chemistry and Physics, Centre for Materials Science, Queensland University of Technology (QUT), 2 George Street, Brisbane, QLD, 4000, Australia

† Electronic supplementary information (ESI) available. See DOI: <https://doi.org/10.1039/d4sc03527e>

‡ Present address: Organic and Carbon Nanomaterials Unit, Okinawa Institute of Science and Technology Graduate University, Japan.

§ Present address: Suzhou Institute for Advanced Research, University of Science and Technology of China (USTC), 215127 Suzhou, China.



reactivity of photoactive molecules. It is commonly known that light irradiation often enables excitation of PI molecules from the ground state ( $S_0$ ) to the singlet excited state ( $S_1$ ), *e.g.* by two-photon absorption in TPP. From there, intersystem crossing to a triplet excited state (often  $T_1$ ) occurs (see Fig. 1a). This process can be followed by a cleavage reaction of the PI into two highly reactive radical fragments that start the polymerization.<sup>4,5</sup> This photochemical cleavage, often assigned to Norrish type I PIs,<sup>4,5,19</sup> is schematically depicted in Fig. 1b and is characterized by an  $\alpha$ -scission of aldehydes and ketones (such as indole, pyrrole, (thio)phenol and aniline<sup>19–21</sup>) into two free radical intermediates. The photoinitiation process proceeds without  $\alpha$ -scission in the case of PIs that behave as, so-called, Norrish type II PIs, such as benzophenone, thioxanthone, or ketocoumarins,<sup>19–23</sup> where co-initiators are also added to the photoresist and two radicals are formed: one on the co-initiator and the other on the PI, respectively (see Fig. 1c). Depending on the nature of the triplet excited state of the Norrish type II PI (mostly  $T_1$ ) and a co-initiator molecule, there are different pathways towards radical formation: hydrogen abstraction, electron transfer or a combination of both, *e.g.* a hydrogen atom transfer (HAT) reaction,<sup>19,24</sup> where carbon-centered radical intermediates<sup>25</sup> are formed *via* photoexcited electron transfer followed by a proton transfer.<sup>22,26</sup> HAT reactions were reported to occur with, *e.g.*, amines or amine synergists,<sup>25</sup> which play the role of a hydrogen donor. Noticeable preference for an electron-based transfer reaction was observed in the case of electron-accepting co-initiators, *e.g.* onium salts (Fig. 1g).<sup>19,27</sup>

The performance of PIs used in 3D laser nanoprinting depends on the radical generation mechanism and the reactivity of the radical formed, as well as the effectiveness of the  $S_0 \rightarrow S_1$  transition, which controls the light absorbance characteristics of photoinitiator molecules. As depicted in Fig. 1, it is modulated by the intersystem crossing (ISC) between singlet and triplet states that depends on the spin-orbit coupling (SOC); it competes with internal conversion (IC) and radiative decay either from a singlet or a triplet state. Therefore, sufficiently fast ISC and long-living triplet states (in the case of Norrish type II PIs) are also required for the radical generation process. In addition, for two-photon based 3D printing of materials, high 2PA cross sections are important.<sup>28</sup>

Among the most sensitive photoresist systems that have successfully been applied in 3D laser nanoprinting, the combination of pentaerythritol triacrylate (PETA) monomer, that is cross-linking upon FRP, with 7-diethylamino-3-thienylcoumarin (DETC) photoinitiator,<sup>1,4,5,11,29,30</sup> is broadly used. DETC has shown high printing efficiency even in formulations with 0.25 and 0.50 wt%<sup>2,4,11,17,29</sup> of the initiator. Higher DETC concentrations are difficult to achieve due to limited solubility in PETA.<sup>2,11</sup> It should be noted that other PIs, specifically Norrish type I, may show similar efficiency in 3D laser nanoprinting as DETC, but for much higher concentrations.<sup>2,4,11</sup> Owing to its chemical structure (depicted in Fig. 1e), DETC behaves as Norrish type II PI<sup>23</sup> and, for photoresists with co-initiators, shows  $N = 2$  photon absorption dependence (using femtosecond lasers with around 800 nm).<sup>4</sup> It was also reported

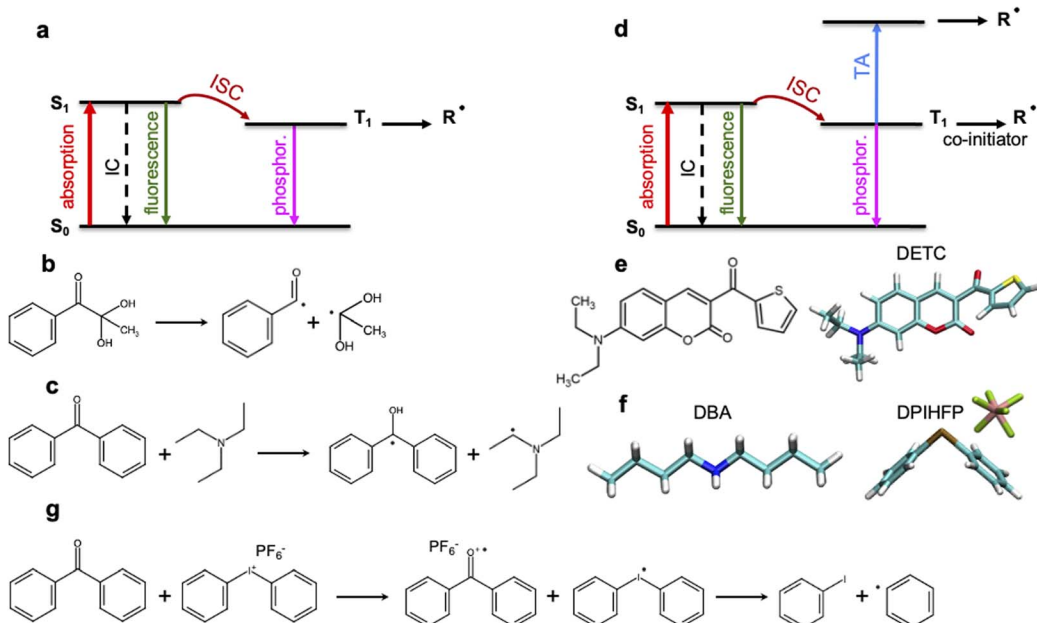


Fig. 1 Schematic representation of the radical formation mechanisms in 3D laser nanoprinting. (a) Norrish type I PIs: photoinduced transition from the ground to the singlet excited state followed by intersystem crossing (ISC) to the lowest triplet state and the formation of radicals. (b) Radical formation via bond cleavage in Norrish type I photoinitiators. (c) Radical formation via hydrogen abstraction from a co-initiator in the presence of Norrish type II PIs. (d) Multiphoton activation of Norrish type II PIs with the formation of radicals either from  $T_1$  (in most cases based on electron transfer process) or from higher triplet states upon triplet state absorption (TA). In TPP, singlet–singlet absorption is often based on 2PA processes. (e) DETC photoinitiator. (f) Dibutylamine (DBA) and diphenyliodonium hexafluorophosphate (DPIHFP) co-initiators. (g) Radical generation during electron transfer from photoinitiator to DPIHFP onium salt. Note: besides phosphorescence, nonradiative decay from the lowest triplet state to the ground state can also occur (not shown in the figure).



to efficiently initiate polymerization in 3D laser nanoprinting without any co-initiator.<sup>4,29</sup> In such a case, absorption of three photons of the same energy was required.<sup>29</sup> Similar  $N = 3$  photon absorption dependence of DETC was reported in other 3D printing studies, which suggested the singlet–singlet transition by 2PA and triplet–triplet transition by 1PA (*i.e.* triplet absorption, TA) to higher triplets<sup>4,31</sup> (schematically depicted in Fig. 1d).  $N$ -photon absorption in both cases was estimated using the “reciprocity law” of the laser power at the polymerization threshold with exposure time.<sup>29</sup> Presently, there is a lack of understanding of the different  $N$ -photon absorption of DETC and the radical formation mechanism with the use of this and similar PIs. This limits the further optimization of initiators for rapid 3D laser nanoprinting.

Here, we report quantum mechanical (QM) calculations of DETC in the ground and excited states to fully elucidate the relevant photophysical processes and photochemical reactions of DETC in the presence and absence of co-initiators such as dibutylamine (DBA) and diphenyliodonium hexa-fluorophosphate (DPIHFP). On this basis, we reveal the radical formation mechanisms upon the multiphoton activation of this PI in 3D laser nanoprinting. In combination with experimental data (3D laser nanoprinting), we analyze the two-photon and three-photon processes in DETC photosensitization and identify pathways for an efficient radical generation. Among the hypothetical radical polymerization mechanisms considered, we explain in detail the intermolecular HAT of DETC with DBA and PETA, as well as demonstrate the impact of the photoinduced electron transfer of DETC in the presence of DPIHFP. We investigate the formation of alkyl radicals by PETA or DBA *via* the reaction of monomers or co-initiators with DETC in higher triplet states. Moreover, we reveal the alkyl radicals formed as the source of the most reactive radical species necessary for FRP of PETA in 3D laser nanoprinting with DETC. We believe that our contribution is important in rationalizing experimental observations that have been poorly understood for many years and in comprehending the designing principles for new PIs for faster 3D printing. Given the limitations and challenges of available QM methods, we attempted to demonstrate possible pathways of radical generation and polymerization initiation.

## Computational details

### Geometry optimization and rates calculation

All calculations were performed using Density Functional Theory (DFT) and Time-Dependent DFT (TD-DFT) methods. Ground state geometry optimization of DETC was performed using temperature annealing approach utilizing the CAM-B3LYP<sup>32</sup> functional with def2-TZVP<sup>33</sup> basis set and Grimme's D3-dispersion correction with Becke–Johnson damping, *i.e.* D3(BJ).<sup>34</sup> Global minimum structures in the ground state were used for excited state calculations (singlet and triplet states), including spectra generation and optimization of excited states using TD-CAM-B3LYP-D3(BJ)/def2-TZVP.  $T_2$  and  $T_5$  excited states could not be properly optimized and therefore were not reported in the paper. Geometry optimization was performed using Gaussian16 Rev. C.01<sup>35</sup> with default ultra-fine grid for

numerical integrations and energy convergence criterion of  $10^{-8}$  Hartree. Calculations were performed both in the gas phase and acetonitrile (ACN) solvent using polarizable-continuum-model (PCM)<sup>36</sup> implicit solvent model, *i.e.*, for excited states non-equilibrium solvation method for all single point calculations and equilibrium PCM procedure for excited states geometry optimizations. All optimized geometries obtained were confirmed with vibrational analysis and, in the case of excited states, confirmed also *via* molecular orbitals analysis. The computational scheme used was optimized considering available experimental data and calculations of 0–0 transition energy  $\nu_{00}$ <sup>37,38</sup> (*i.e.*, between vibrational states of the ground and the first singlet excited electronic states), as described in Section 2 in ESI.† The quality of the TD-DFT setup for vertical excitation energies of DETC was confirmed by the GW (one-body Green's function with the dynamically screened Coulomb interaction) approximation and Bethe–Salpeter equation (BSE)<sup>39,40</sup> implemented in TURBOMOLE v7.4<sup>41</sup> (see Tables S2 and S22†). Analysis of the charge (electron and hole) differences between the ground and excited states were performed using Multiwfn (version 3.6) analyzer.<sup>42</sup>

Spin-unrestricted DFT scheme (U)CAM-B3LYP-D3(BJ) was used for the optimization of radicals and biradicals considered in this study. All thermodynamic quantities were computed after vibrational analysis using implicit ACN (PCM model) using (U)CAM-B3LYP-D3(BJ)/def2-TZVP level of theory in Gaussian16. The reaction temperature of 298 K and pressure of 1 atm were considered. Rates for IC, ISC and Reversible Intersystem Crossing (RISC) were calculated employing the Franck–Condon approximation (FC)<sup>43</sup> (see details in ESI†) using MOMAP 2022A (2.3.3)<sup>44–49</sup> (Molecular Materials Property Prediction Package). TD formalism was used. The radiative rate constants, *i.e.*, fluorescence and phosphorescence, were calculated using DETC optimized singlet and triplet state structures at ACN and in the gas phase with MOMAP. Adiabatic Hessian (AH) potential energy surfaces (PES) model within TD-DFT was used for the computation of all the radiative rates.

### Absorption spectra calculation

1PA,<sup>50</sup> 2PA<sup>51,52</sup> and three-photon absorption (3PA)<sup>52,53</sup> spectra were computed both in the gas phase and implicit ACN and PETA (PCM model) using TD-CAM-B3LYP-D3(BJ)/def2-TZVP in Dalton 2020.0<sup>54</sup> and Gaussian16 Rev. C.01 (only 1PA). 2PA and 3PA spectra were calculated considering a single laser beam, linearly polarized light with parallel polarization (as experimental set-up); transition moments were defined on two- and three photons of the same frequency, respectively. Spectra were plotted using half width at half maximum (HWHM) of 0.1 eV and Lorentzian type broadening function. TA spectra were computed with TD-(U)CAM-B3LYP-D3(BJ)/def2-TZVP approach in ACN starting from the  $T_1$  optimized geometry, obtained *via* TD-DFT using Gaussian16. To evaluate the intensities of transitions between two vibronic states, the Franck–Condon principle was employed considering that the nuclear positions are mostly unaltered by the electron jump which takes place during the electronic transition.



Vibrationally resolved singlet and triplet spectra were computed at TD-DFT level of theory within the Franck-Condon<sup>55,56</sup> (FC) approximation at 100 K with Adiabatic Hessian (AH-G16) as PES model. Spectra were plotted with HWHM of 80 cm<sup>-1</sup> (*i.e.*, 0.01 eV), convergence factor of  $1.0 \times 10^{-4}$  a.u. and Lorentzian type broadening function. The energy transitions from vibrational levels of the initial state to the vibrational levels of the final state, *i.e.*, higher triplet excited state, were considered. The strength of a particular transition was obtained as a result of the population of that state and the overlap between initial and final vibrational wavefunctions for that transition. Spectra were computed using Dynavib<sup>57,58</sup> in implicit ACN with TD-CAM-B3LYP-D3(BJ)/def2-TZVP level of theory, starting from the lowest triplet excited state and higher triplet excited states. Due to significant geometry differences between T<sub>1</sub> and T<sub>3</sub> states in ACN (see Fig. S11†), which go beyond the harmonic vibrational potentials within FC approximation, the corresponding spectrum could not be generated. Several different models, employed for the computation of the PES, *i.e.* time-independent and -dependent FC and non-Condon simulation including Duschinsky effect<sup>59</sup> and FC and non-Condon simulations based on linear coupling model (LCM) model,<sup>60,61</sup> have not improved the output.

## Experiments

To investigate the polymerization laser threshold of various DETC-containing resists, the previously reported setup<sup>11</sup> was applied. Herein, a mode-locked femtosecond laser oscillator (Mai Tai HP, Spectra-Physics), working at  $R_p = 80$  MHz repetition rate and  $\lambda = 820$  nm center wavelength, a microscope lens (Leica HCX PL APO 100x/1.4-0.7 Oil CS) for beam focussing in oil-immersion mode, and an acousto-optic modulator (AA MT80-A1.5-IR) were utilized. The resists were prepared by adding 7-diethylamino-3-thenoylcoumarin (DETC; 30 µmol), dibutylamine (DBA; 7.5 µmol, 15 µmol, 30 µmol, 60 µmol, and 120 µmol), or diphenyliodonium hexafluorophosphate (DPIHFP, 15.6 µmol, 31.2 µmol, and 62.4 µmol), respectively, to pentaerythritol triacrylate (PETA; 2 g) in a vial under constant stirring. DETC was purchased from Exciton. DPIHFP (>97.5% purity) was purchased from TCI. PETA (technical grade) and DBA (99.5% purity) were purchased from Sigma-Aldrich.

To measure the laser polymerization threshold for a given exposure time  $t_{exp}$ , separated points of the photoresist were illuminated with different laser powers  $P$ . The lowest laser power, which still forms a visible polymer dot<sup>29</sup> after development with acetone is then defined as the laser polymerization threshold power  $P_{th}$ .

## Results and discussion

### One-photon and multiphoton absorption

Quantum mechanical calculations of photochemical processes and photoreactivity of molecules are either computationally very expensive or not accurate enough, *i.e.* *via* the use of multi-reference based post-Hartree-Fock methods or DFT formalism, respectively. To calibrate the accuracy of the computational

protocol a set of DFT and GW approximation Bethe-Salpeter equation (GW-BSE)<sup>39,40</sup> calculations were performed and compared to available experimental data (Sections 1, 2 and 7 in ESI†) as well as several wavefunction-based methods (Section 5 in ESI†). Considering reported 1PA and emission data of DETC in PETA<sup>4</sup> and in acetonitrile (ACN) (see Fig. S3†), we have calculated 1PA spectra using linear-response TD-DFT with long-range corrected CAM-B3LYP<sup>32</sup> to describe the one-photon process (Fig. 2a, S2, and Table S1†). The calculated 1PA spectrum of DETC in ACN, as well as the excitation energies computed with GW-BSE approach and the values of  $E_{0-0}$  energies ( $\nu_{00}$ <sup>37,38</sup> *i.e.*, between the ground vibrational states of the two electronic states considered) show good agreement with the experiment. The 1PA spectrum of DETC (visualized in Fig. 2a) indicates the blue-shifted absorption maximum (by ~60 nm) in comparison with the measured spectrum of DETC in ACN (359.30 nm vs. 421 nm). However, the consideration of vibronic effects modulates the redshift in spectra, being closer to the experiment (see Fig. S2 and S3†). The computation of absorption and emission energies has also been performed while including corrected linear response (CLR)<sup>62</sup> and state specific (SS) corrections for the solvation model, *i.e.*, external iteration (EI).<sup>63,64</sup> This data is reported in Tables S6–S8.† The value of  $E_{0-0}$  is 439.04 nm (2.82 eV) with CLR instead of 407.44 nm (3.04 eV) with LR, indicating an impact of state-specific formulations in TD-DFT. The experimental Stokes shift of DETC in ACN is 460.50 nm (2.69 eV, see Table S3†), which could be well reproduced using an optimized computational protocol. The calculated emission characteristics of DETC are consistent with the reported literature data as well, *i.e.*, the fluorescence rate in ACN is  $4.30 \times 10^8$  s<sup>-1</sup> (Table S20†), while the experimentally reported values in toluene and methanol (22) are  $\sim 2-4 \times 10^9$  s<sup>-1</sup>.

For the estimation of the character of vertical excitations of DETC, the transition orbitals and the analysis of its charge transfer (CT) characteristics<sup>65</sup> have been performed. They are depicted and described in detail in Section 3 in ESI† where the comparison with the spin-component scaled coupled cluster (SCS-CC2) method is provided. From Table S12,† it is clearly seen that CT in DETC is rather strong: transitions S<sub>0</sub> → S<sub>1</sub>, S<sub>0</sub> → T<sub>1</sub> and S<sub>0</sub> → T<sub>7</sub> exhibit less negative  $t$  parameters, suggesting higher CT, while the remaining transitions have highly negative  $t$  values, indicating a mixed character of CT and local exciton (LE) transitions, as depicted in Fig. S6.† The change of the electronic structure of DETC following light-induced transitions, the molecular orbitals (MOs) and the electron density delocalization over its  $\pi$ -conjugated system are depicted in Fig. S4–S7† and explained in detail in Section 3 in ESI†.

The quality of calculated 1PA spectra directly impacts the accuracy of 2PA spectra necessary to evaluate the efficiency of PI in TPP. Even if 1PA and 2PA involve strictly defined transitions between ground and excited states of a molecule, the underlying light-induced processes are different in nature and follow different selection rules, *e.g.*, in terms of symmetry of the state and the electric dipole transitions. Therefore, not all molecules are both 1PA and 2PA active, however, the calculated 2PA spectrum of DETC (Fig. 2b) reveals its 2PA activity. The 2PA spectrum of DETC in ACN shows maximum absorption at



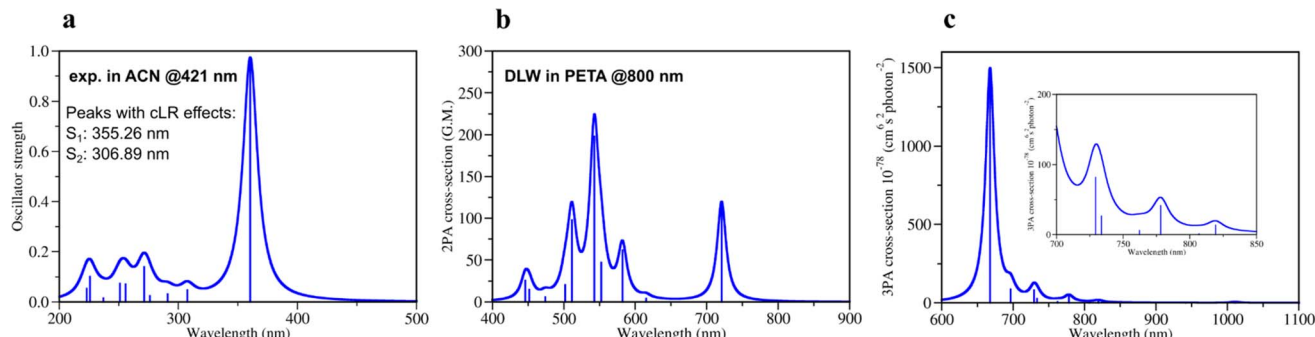


Fig. 2 Theoretically calculated spectra of DETC using TD-CAM-B3LYP/def2-TZVP: (a) one-photon absorption spectrum and (b) two-photon absorption spectrum in acetonitrile (PCM implicit solvent model) (c) three-photon absorption spectrum in the gas phase with the insertion of the zoomed spectrum in the region 700–850 nm. All spectra were obtained starting from the optimized ground state geometry of DETC using CAM-B3LYP-D3(BJ)/def2-TZVP level of theory. Spectra were plotted using half width at half maximum (HWHM) of 0.1 eV and Lorentzian type broadening function. vibrationally-resolved 1PA spectrum is depicted in Fig. S2.† Note: DLW denotes direct laser writing.

720.84 nm with the highest calculated cross-section at this wavelength of 119.0 GM (Fig. 2b, and Table S13†). The spectrum possesses a blue-shift in comparison to experiments<sup>16,66</sup> which is a repercussion of the blue-shift in the 1PA spectrum (Fig. 2a), where the calculated and measured absorption maximum are located at 359.30 nm and 421.00 nm, respectively (see Table S1 and Fig. S3†). The calculated 2PA cross-section is higher than the recently reported 2PA cross-sections of DETC in dichloromethane (82 GM)<sup>16</sup> and dimethyl sulfoxide (40 GM)<sup>66</sup> at 780 nm and 800 nm, respectively. The calculated 2PA using the implicit representation of these solvents is reported in Fig. S8.† Considering spectral shifts in the 1PA spectra, they still demonstrate good correlations.<sup>2–5,30,31</sup> Here, we note that the direct comparison of 2PA cross-sections between experiment and theory is challenging due to the high sensitivity of cross-section values to the variety of experimental parameters and referencing methods, as well as the selection of parameters for the calculation of theoretical spectra<sup>51</sup> and consideration of environmental, *i.e.*, solvent, effects. Moreover, experimentally reported 2PA cross-sections of DETC differ between 82 GM and 40 GM, depending on the solvent and measurement technique (two-photon induced fluorescence and z-scan, respectively).<sup>16,66</sup> Several factors contribute to the discrepancy in these values. Firstly, the determination of 2PA absorption cross-sections using two-photon fluorescence has an accuracy limited to 8–10%.<sup>67</sup> Secondly, it is known that z-scan data typically underestimates 2PA cross-section by up to a factor of 2.5–5,<sup>68</sup> bringing the true value measured *via* z-scan closer to 100–200 GM. Finally, it is important to keep in mind that neither of the mentioned experimental studies of DETC considered the potential for higher-order absorption processes.

To evaluate the possibility for DETC to simultaneously absorb three photons during singlet–singlet 3PA, the respective spectrum in the gas phase was calculated (Fig. 2c, and Table S14†). A peak related to  $S_0 \rightarrow S_1$  transition was found to be at 1010.74 nm with a 3PA cross-section of  $5.6 \times 10^{-78} \text{ cm}^6 \text{ s}^2 \text{ photon}^{-1}$ . The cross-section values related to transitions between  $S_0$  and higher excited states using the laser wavelength of 819–778 nm (*i.e.*,  $S_0 \rightarrow S_3$ ,  $S_0 \rightarrow S_4$  and  $S_0 \rightarrow S_5$ ) are in the

range of  $1–42 \times 10^{-78} \text{ cm}^6 \text{ s}^2 \text{ photon}^{-1}$ . Therefore, theoretical calculations indicate that DETC might be prone to instantaneously absorb three photons, leading to very high singlet excited states. Since such highly excited states tend to relax rapidly *via* conical intersections (typical vibrational frequencies of modes coupled to the electronic transition have been calculated to be on the order 20 THz, *i.e.*, 50 fs),<sup>69</sup> which are unstable, they will decay to the lowest singlet excited state. Since the  $S_1$  state is typically reached *via* 2PA using femtosecond lasers, no additional photons (*i.e.*, more than 2) would be detected in the nonlinearity fits of the threshold laser power *versus* exposure time in the TPP (discussed further). Due to the same reason, 3PA processes may not be observed at all using fluorescence as the detection system, since two- and three-photon induced fluorescence quantum yields can significantly vary due to channel branching in the excited state manifold (singlet and/or triplet in nature) of dye molecules. It has been shown for fluorene derivatives that shifting the excitation wavelength from the UV to the near-infrared region significantly increases the contribution of three-order processes compared to first and second order.<sup>70</sup> 3PA processes were not considered in the fits to the z-scan data of DETC.<sup>66</sup> Therefore, accurate excitation wavelength z-scan data would be needed to simultaneously analyze contributions both from two- and three order processes.<sup>71</sup> To the best of our knowledge, no such analysis has been performed on DETC, likely due to experimental challenges such as contributions from self-phase modulation, impulsive stimulated Raman scattering, wavelength-dependence of higher-order processes *etc.*

### Multiphoton 3D laser nanoprinting using DETC

To analyze the various aspects of DETC performance in 3D laser nanoprinting, we investigate different photoresist compositions, *i.e.*, with pure DETC as the photoinitiator and after the addition of the co-initiators: DBA or DPIHFP. Both co-initiators were considered since they were demonstrated to decrease the threshold laser power for rapid 3D laser nanoprinting.<sup>11</sup> Here, DBA was found to be more efficient than triethylamine, which is a more typical amine-based co-initiator than DBA. Moreover, no



lowering in the degree of co-sensitization due to volatility, side reactions or concentration-induced absorption changes, reported for other co-initiators based on tertiary amines, have been noticed.<sup>72</sup> Point exposure experiments were performed using PETA as a monomer to evaluate the initiation mechanism of these photoresist compositions. In Fig. 3, we observe significant differences in the experimental threshold laser power *vs.* exposure time, *i.e.*, different scaling behaviors, for all resist systems. Here, the  $N \sim 2$  photon dependence<sup>11</sup> is solely observed for resists comprising DETC and DPIHFP (Fig. 3a). As previously reported, pure DETC shows  $N \sim 3$  scaling.<sup>29</sup> No changes in scaling after the addition of the DBA as a co-initiator are observed (Fig. 3b).

The underlying mechanisms for radical generation in all these cases may proceed *via* photoinduced HAT, electron transfer or TA. With onium salts, DETC is most likely to participate in electron transfer (ET) and/or energy transfer from the photoexcited sensitizer to the iodonium cation, followed by the rapid decomposition of the resulting unstable diaryliodine radical that prevents back electron transfer and renders the overall process irreversible.<sup>27,58</sup> HAT was reported for DETC (and similar ketocoumarins) with amine-based co-initiators.<sup>4,73,74</sup> Since ET happens on the picosecond timescale,<sup>75</sup> it is faster than HAT, which was shown to be a diffusion modulated process.<sup>76</sup> This agrees with the observation from 3D printing of PETA: the electron transfer process between DETC and DPIHFP results in the 2PA-initiated polymerization. The HAT reaction between DBA and DETC, involving a two-step intermolecular transfer (see Fig. 1c), should not occur from the  $T_1$  excited state of DETC, because the nonlinearity does not decrease from  $N = 3$  to 2, as observed for onium salt. As mentioned above, 3PA of DETC has not been reported up to date, however such a process may well occur, in addition to 2PA, as was reported for other chromophores.<sup>77</sup> This may be the reason why the nonlinearity

dependence is slightly higher than  $N = 3$ . Such 3PA with 775–800 nm may excite DETC to  $S_3$ – $S_5$  states. However, due to fast decay to the  $S_1$  excited state, higher singlet states of DETC do not participate in the radical formation. Therefore, TA, resulting in highly reactive DETC triplet states, seems to be more probable to occur. This should allow the polymerization reaction, while the radical reaction channel from the  $T_1$  state of DETC is hindered due to diffusion-controlled reactions, particularly in high-viscosity resins.<sup>76</sup>

We have compared the reactivity of DETC (in the  $T_1$  state) in HAT reaction with DBA in terms of reaction energy profile and transition state that leads to the radical formation according to Fig. 1c. Obtained energies and reaction mechanisms are depicted in Fig. S19 and Table S25.<sup>†</sup> HAT reaction from co-initiator to DETC is not spontaneous from  $S_0$  state of DETC since the Gibbs free energy is 48.19 kcal mol<sup>-1</sup> in ACN. Upon photoactivation of DETC and the formation of the  $T_1$  state, the Gibbs free energy lowers to 0.44 kcal mol<sup>-1</sup> and the energy barrier (from the transition state calculation) is 6.72 kcal mol<sup>-1</sup>. Thus, it allows HAT with the rate of  $7.33 \times 10^7$  s<sup>-1</sup>, calculated employing the Eyring equation<sup>78</sup> at room temperature and pressure, in ACN. Therefore, HAT between DBA and DETC in the  $T_1$  state should theoretically occur, resulting in the  $N \sim 2$  in 3D printing, however, it is not observed in printing conditions. Recently, Xue *et al.*<sup>79</sup> have reported that the reaction of benzylidene ketone PIs with the amine-based co-initiators is predominantly controlled by material diffusion rather than by an activation process. We believe this may be the reason why resists with DBA do not show two-photon scaling during 3D printing of PETA using DETC, reported in Fig. 3b. The QM calculations of HAT reaction between DETC and DBA are presented in Section 8 in ESI.<sup>†</sup>

Consequently, bimolecular radical initiation shows a dependence on the exposure time and the concentration of the co-

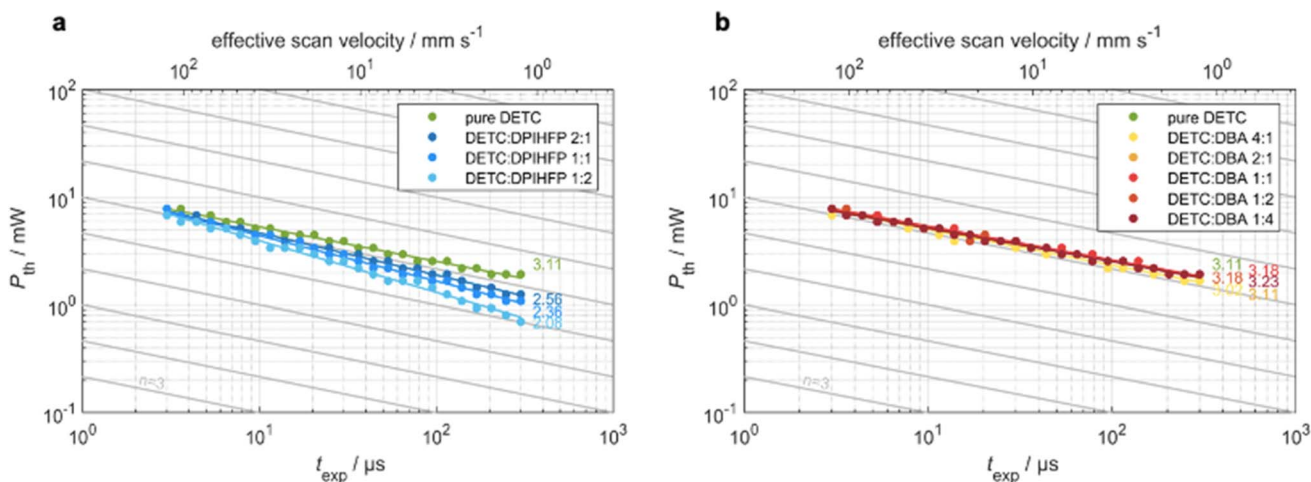


Fig. 3 Measured threshold laser power versus exposure time on a double-logarithmic scale for resist systems with only DETC as initiator as well as resist systems with DETC and additionally (a) diphenyliodonium hexafluorophosphate (DPIHFP) and (b) dibutylamine (DBA) co-initiators in varying ratios. The slopes of the fits indicate the nonlinearity of the resist system. The gray lines are guides to the eye with a slope of  $N = 3$  as expected for the DETC system. (a) With increasing concentration of DPIHFP, the nonlinearity changes from  $N = 3$  to  $N = 2$ . (b) Independent on the concentration of DBA, the nonlinearity stays at  $N = 3$ .



initiator (Fig. 3a). For longer exposure times or higher concentrations of DPIHFP, the bimolecular mechanism dominates over TA, however, it lowers the sensitivity of printing.

### Photophysical processes of DETC upon singlet–singlet excitation

The photosensitization of PIs can be activated in  $T_1$  triplet state (see Fig. 1), which, in principle, is achieved when SOC, thus, the ISC from singlet to triplet excited states is high enough. The direct SOC between the  $S_1$  state of DETC and the  $T_1$  state is  $0.97\text{ cm}^{-1}$  and happens with an ISC rate of  $8.84 \times 10^4\text{ s}^{-1}$  (see Table 1). This observation suggests that the ISC pathways *via* conical intersections and other triplet states would impact the photoactivation of DETC. Indeed, after geometry optimization (see description in ESI<sup>†</sup>), analysis of electronic properties and calculation of SOC and ISC rates involving two singlet states ( $S_1$  and  $S_2$ ) and several triplet ( $T_1$ ,  $T_3$ ,  $T_4$ ,  $T_6$ , while  $T_2$  and  $T_5$  did not converge) states of DETC, we can conclude that direct ISC between  $S_1 \rightarrow T_1$  should not be the main pathway for the formation of the  $T_1$  state. From the Jablonski diagram of DETC in ACN, depicted in Fig. 4, it can be stated that upon absorption from the ground state,  $S_1$  excited state couples strongly to the  $T_3$  excited state with the SOC of  $7.55\text{ cm}^{-1}$  (see Table 1), resulting in a fast and efficient ISC rate of  $\sim 1.72 \times 10^8\text{ s}^{-1}$ . Here, we have to note several important observations. Firstly, the  $T_3$  state, optimized in ACN, shows a twist of  $-97.7^\circ$  of the thiophenyl group of DETC with respect to the core (dihedral angle C9–C8–C11–C17, see Fig. S1, S10, and S11<sup>†</sup>). Such a perpendicular-like position, as previously noted by Tozer *et al.*<sup>80</sup> is unnatural for the DETC molecule and contrasts with the dihedral angle in the ground state geometry of  $-45.9^\circ$ . It is not present in the case of  $T_3$  computed in the gas phase, where the twist is only by  $-41.45^\circ$ . Such strong structural differences were not observed between the ground state and the  $S_1$  geometries optimized in ACN and gas phase (see Fig. S11<sup>†</sup>). Secondly, we encountered the poor convergence of the correlation function in the computation of ISC rates between  $T_3$  and  $S_1$ , which were both optimized in implicit ACN (see explanation in Section 6 in ESI, Table S19a and Fig. S16<sup>†</sup>). This suggests an influence of the polarization included by the implicit solvent and subtle (complex) electronic nature of higher excited states of DETC that could not be resolved with the LR-TD-DFT. Higher level methods and the consideration of nonequilibrium conditions might be necessary, however it is beyond the present investigations. The ISC rate successfully converged utilizing the  $T_3$  state optimized in the gas phase (see Fig. S16<sup>†</sup>), therefore it was used for the computation of photophysical rates of DETC (Table 1).

The energy difference between the  $S_1$  and  $T_3$  states in ACN is  $-0.12\text{ eV}$ , as depicted in Fig. 4, *i.e.*, the adiabatic  $T_3$  state lies slightly higher than the  $S_1$  state. According to the calculation of the vertical energy differences by several wavefunction-based methods using the optimized structures from TD-DFT (see Tables S16 and S17<sup>†</sup> with the respective explanation), the  $T_2$  state in ACN is closer to the  $S_1$  state, but both  $T_2$  and  $T_3$  are still higher than  $S_1$ . However, all post-HF-based energies obtained

**Table 1** Nonradiative and radiative rates. Internal conversion (IC), intersystem crossing (ISC) and reverse ISC (RISC) of DETC in implicit ACN and gas phase calculated with TD-CAM-B3LYP-D3(BJ)/def2-TZVP level of theory. IC, ISC and RISC rates ( $\text{in s}^{-1}$ ) were calculated using nonadiabatic coupling matrix elements (NACME, in au), spin–orbit-coupling (SOC, in  $\text{cm}^{-1}$ ), considering non-equilibrium solvent effects, and reorganization energy ( $\lambda$ , in eV) using approach described in methods and explained in ESI (Section 6). Radiative rates (fluorescence and phosphorescence) of DETC in implicit ACN were calculated with the same level of theory using  $\Delta E$  (in eV) and lifetime (in s). NA refers to “not available” and in the case of the rate signifies that the correlation function was not converged. All rates are calculated considering equilibrium states

	Nonradiative rate	Rate ( $\text{s}^{-1}$ )	NACME (au)	$\lambda$ (eV)
IC	$S_1 \rightarrow S_0$	$1.60 \times 10^8$	0.009	0.205
	$S_2 \rightarrow S_0$	NA	0.004	1.341
	$T_6 \rightarrow T_1$	$1.25 \times 10^{10}$	0.006	0.171
	$T_4 \rightarrow T_1$	$4.50 \times 10^{10}$	0.006	0.478
	$^aT_3 \rightarrow T_1$	$1.76 \times 10^{11}$	0.003	0.572
	Nonradiative rate	Rate ( $\text{s}^{-1}$ )	SOC ( $\text{cm}^{-1}$ )	$\lambda$ (eV)
ISC	$S_1 \rightarrow T_1$	$8.84 \times 10^4$	0.97	0.027
	$^aS_1 \rightarrow T_3$	$1.72 \times 10^8$	7.55	0.316
	$S_1 \rightarrow T_4$	$3.94 \times 10^6$	4.49	0.201
	$S_1 \rightarrow T_6$	$6.56 \times 10^6$	9.51	0.336
	$S_2 \rightarrow T_1$	$6.33 \times 10^8$	22.96	0.474
	$^aS_2 \rightarrow T_3$	$1.57 \times 10^{11}$	26.96	0.390
	$S_2 \rightarrow T_4$	$7.94 \times 10^{10}$	25.81	0.429
	$S_2 \rightarrow T_6$	$5.75 \times 10^6$	9.43	0.960
	$T_1 \rightarrow S_0$	$8.64 \times 10^4$	2.16	0.181
	$T_1 \rightarrow S_1$	$5.18 \times 10^4$	0.80	0.021
	$^aT_3 \rightarrow S_1$	$5.39 \times 10^9$	5.47	0.284
	$T_4 \rightarrow S_1$	$2.44 \times 10^9$	7.68	0.600
RISC	$T_6 \rightarrow S_1$	$1.38 \times 10^8$	2.09	0.362
	$T_1 \rightarrow S_2$	$3.59 \times 10^6$	15.52	0.351
	$^aT_3 \rightarrow S_2$	$5.34 \times 10^6$	6.41	0.384
	$T_4 \rightarrow S_2$	$6.89 \times 10^6$	4.30	1.974
	$T_6 \rightarrow S_2$	$3.52 \times 10^8$	2.35	0.712

Radiative rate	Rate ( $\text{s}^{-1}$ )	$\Delta E$ (eV)	Lifetime (s)
Fluorescence	$4.30 \times 10^8$	3.04	$2.33 \times 10^{-9}$
Phosphorescence	$7.69 \times 10^{-1}$	2.09	1.30

<sup>a</sup>  $T_3$  was optimized in the gas phase, while  $S_1$ ,  $S_2$  and  $T_1$  in ACN. The energy gap considered was computed between  $T_3$  and  $S_1$ ,  $S_2$  or  $T_1$  in ACN and SOC in ACN.

represent only the differences in the vertical energies, while TD-DFT data are for the optimized states. Unfortunately, the  $T_2$  state of DETC could not be reliably optimized in TD-DFT in both ACN and the gas phase to evaluate the competitiveness of the ISC *via*  $S_1 \rightarrow T_2$  transition. We assume that this fact may be connected to the limitations of the LR-TD-DFT for this specific state, *i.e.*, the transition electron density of  $T_2$  (as well as  $T_5$ , which could not be obtained) is differently captured in TD-DFT than in SCS-CC2 in ACN (see Fig. S7<sup>†</sup>). Electron density differences for other states of DETC are more consistent within TD-DFT and SCS-CC2, therefore, we rely on them.

The ISC between  $S_1 \rightarrow T_3$  shows dominant  $\pi\pi^* \rightarrow \pi\pi^*$  character (60% in the gas phase), supporting El-Sayed rule<sup>81–83</sup>



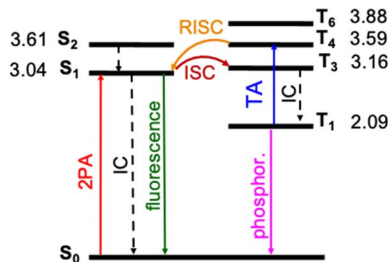


Fig. 4 Jablonski diagram of DETC. Excited states were optimized in acetonitrile (PCM model) using TD-CAM-B3LYP-D3(BJ)/def2-TZVP level of theory. Adiabatic energy values, including zero-point-energy (ZPE) correction, are reported in eV. Rates of transitions between different states, calculated using electronic structure parameters, obtained with TD-DFT approach, are listed in Table 1. Note: besides phosphorescence, nonradiative decay from the lowest triplet state to the ground state can also occur (not shown in the figure).

for ISC processes. It also indicates vibronic spin-orbit interactions that increase the SOC.<sup>84</sup> Since SOC is impacted by the way the solvent effects are included (see Table S18†), for all calculations we use the SOC with the included non-equilibrium effects for the solvent, resulting in data that correlates better with experiments (Table S19†). Even if such SOC value is lower than in the gas phase, the ISC rate, considering the  $\Delta E(S_1-T_3)$  of  $-0.12$  eV is still reasonable ( $1.72 \times 10^8$  s $^{-1}$ ), competing with IC ( $1.60 \times 10^8$  s $^{-1}$ ) and fluorescence ( $4.30 \times 10^8$  s $^{-1}$ ). We have to point out that the parameters described and the shape of molecular orbitals during the transitions are strongly dependent on molecular vibrations, vibronic couplings and solvation effects, resulting in the mixing of  $n\pi^*$  and  $\pi\pi^*$  states, which is observed for  $S_1 \rightarrow T_3$ . Therefore, more detailed analysis of transition dynamics and subtle differences should be accessed by a higher level of theory and non-adiabatic molecular dynamics to obtain more realistic values. This was not in the scope of the current investigation.

Once DETC reaches  $T_3$  state, it undergoes fast IC decay to the  $T_1$  state with the rate of  $1.76 \times 10^{11}$  s $^{-1}$  (Table 1). The lifetime of  $1.16 \times 10^{-5}$  s (11.6  $\mu$ s) for the non-radiative decay of  $T_1$  (*i.e.*, ISC  $T_1-S_0$ ) allows other processes to occur. Charge density analysis, *i.e.*, the localization of electron-donating (hole) and electron-accepting (electron) parts of  $T_1$  excited state of DETC demonstrates the activation of carbonyl moiety (atoms C11–O12, see areas in green in Fig. S6†) with higher local electron densities that should participate in electron transfer and HAT. Therefore, DETC should be prone to attack the amine-based co-initiator permitting H-atom transfer reaction. However, as discussed above, it is hindered in the present study. This is shown by the deviation of nonlinearities far away from 2 that is expected for the typical Norrish type II PIs after PI activation to the  $T_1$  state.

### Multiphoton activation of DETC to higher triplet states

DETC initiates FRP in the absence of any co-initiator molecule with the use of three photons at  $\sim 800$  nm<sup>2,4,11,29,30</sup> (see Fig. 3). It is an interesting observation since DETC ketyl radicals alone are less active: the bond dissociation energy of O–H bond in ketyl radicals is relatively low (*e.g.* 16 kcal mol $^{-1}$  in acetone<sup>85</sup>). This

indicates a different pathway for PI photoreactivity in TA, shifting the electronic state of DETC to higher triplet states. To define which triplet excited state can be reached by the upcoming third photon during 3D printing, a one-photon based triplet-triplet excitations in ACN were calculated (listed in Tables S21, and S22†).

The presence of a peak located at 815 nm (see Table S21†), *i.e.* value close to the fs laser wavelength used in experiment, confirms the TA absorption of photons in the  $T_1$  state. However, such a treatment neglects the influence of vibronic coupling of the electronic transition, providing a simplified view of absorption spectra. To overcome this limitation and to assign the transition to the activated triplet state, vibrationally resolved triplet spectra<sup>55</sup> for several transitions between  $T_1 \rightarrow T_n$  ( $n = 4, 6$ ) were computed (see Fig. S17†). Among spectra obtained, the transition  $T_1 \rightarrow T_4$  overlaps with the experimentally used photon energy (see Fig. 5). Therefore, the excitation of DETC in 3D printing should allow the transition of the PI most probably to the  $T_4$  state with the charge density difference depicted on the upper left panel in Fig. 5. Interestingly, the oscillator strength of TA at the printing wavelength is much higher for DETC than for other Norrish type II PIs.<sup>18,31</sup> Fast TA may also be the reason why the HAT reaction with DBA (from  $T_1$  of DETC) is hindered, indicating a high probability of the DETC photoreactivity from higher triplet states. Note that in such states DETC may also decay to the lowest triplet state (calculated IC $_{T_4-T_1}$  is  $4.50 \times 10^{10}$  s $^{-1}$ , see Table 1) or return to singlet states *via* reverse inter-system crossing (RISC). RISC rates of DETC from the  $T_3-T_4$  states (*e.g.* rate of  $5.39 \times 10^9$  s $^{-1}$  for  $T_3 \rightarrow S_1$ ,  $2.44 \times 10^9$  s $^{-1}$  for  $T_4 \rightarrow S_1$ ), might compete with IC permitting deactivation of DETC, *i.e.* its depletion, which was also reported to occur using the second inhibition laser source of 800 nm (femtosecond)<sup>4</sup> and 808 nm (continuous).<sup>24</sup>

### Mechanisms of radical formation

To further estimate the radical formation of DETC in high triplet states, initiating FRP, several mechanisms were

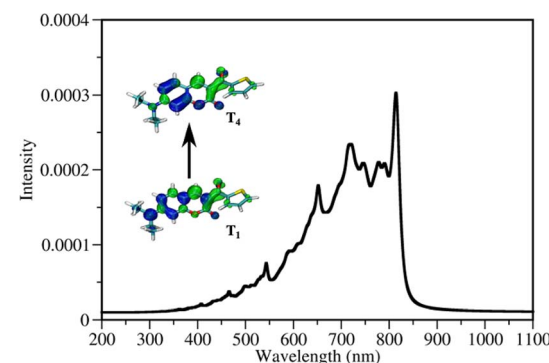


Fig. 5 Vibrationally resolved triplet–triplet spectrum of DETC for its  $T_1 \rightarrow T_4$  transition employing  $T_1$  as starting geometry. Visualization of the electron density difference in  $T_1$  and  $T_4$  excited states compared to the electronic structure of DETC in the ground state is reported in the inset. Electron donating regions, *i.e.* holes, and electron accepting, *i.e.* electrons, are marked in blue and green, respectively. An isovalue of 0.002 a.u. was used for visualization.



considered. Similarly, to the formation of aminoalkyl radicals of DBA (see Fig. 1c) photoactivated H-abstraction reaction<sup>85</sup> was calculated for DETC (see Section 9.1). Higher C–H activation possibility with lower bond dissociation enthalpy (BDE) is triggered by PI in high triplets (BDE lower than 8.8 kcal mol<sup>−1</sup> in comparison to 82 kcal mol<sup>−1</sup> in S<sub>0</sub>, see Table S26†). However, the process is not spontaneous (see the Gibbs free energy values in Table S27†) and could not even compete with spontaneous internal conversion (Table 1), disabling the radical formation *via* C–H bond breaking, depicted in Fig. S21a.† This is also the reason for the hindered formation of the hypothetically highly reactive DETC biradicals that were suggested to occur for similar chromophore molecules<sup>43,86–88</sup> (see Section 9.3 in ESI†). Indeed, if such biradicals are formed, they should initiate FRP from an excited state of DETC (higher than T<sub>3</sub>) spontaneously (see Section 10 in ESI†). However, neither such intramolecular HAT was confirmed experimentally, nor the calculated Gibbs free energies *vs.* nonradiative decay should permit it. Unfortunately, transition state calculations using higher triplet states of DETC could not be obtained to further predict the kinetics of this reaction. Interestingly, the formation of DETC radicals *via* photolysis should in theory be spontaneous (Section 9.2). The cleavage of N14–C15, C15–C16 or C8–C11 bonds of DETC (see Fig. S21c†) is thermodynamically more favorable in T<sub>4</sub> (Table S29†) with the Gibbs free energy even −26.96 kcal mol<sup>−1</sup> in the case of N14–C15 bond cleavage. However, the entropic contribution to the Gibbs free energy, calculated using the vibrational frequencies within harmonic approximation and considering implicit ACN, is relatively high, *i.e.*, of around 0.05 kcal mol<sup>−1</sup> K<sup>−1</sup>. This may be impacted by explicit treatment of solvent and anharmonic effects, therefore, experimental validation of DETC photolysis is essential. Such a reaction should also be kinetically accessible to compete with spontaneous IC or RISC processes, which happen with the rate of  $4.50 \times 10^{10}$  s<sup>−1</sup>/1.25  $\times 10^{10}$  s<sup>−1</sup> and  $2.44 \times 10^9$  s<sup>−1</sup>/1.38  $\times 10^8$  s<sup>−1</sup> from T<sub>4</sub>/T<sub>6</sub> excited state, respectively (see Table 1). Fig. S21† illustrates the key finding regarding the formation of DETC radicals according to the mentioned reaction mechanisms. This study indicates that if DETC spontaneously form reactive radicals for FRP in 3D printing, they may originate from photolysis. Moreover, the formation of the DETC ketyl radical (shown in Fig. 1c) is possible, however, it is less reactive than other possible species (Table S32† and ref. 89 and 90).

Since the photoresist contains also PETA monomers, we have investigated the impact of DETC on the radical formation directly by PETA. The mechanism of PETA radical formation should be similar to the reaction between DETC and the DBA co-initiator (Section 8 in ESI†). The intermolecular HAT should involve the C–H bond cleavage of the alkyl chain of PETA upon DETC attack *via* the carbonyl functional group (see Fig. 6). C–H bond cleavage of PETA without DETC possesses high BDE (the lowest value is of 84.05 kcal mol<sup>−1</sup>, see Table S23 and Fig. S18†) and it requires a higher number of photons to enable the 3D printing.<sup>2,4,29</sup> (in general, such printing loses its resolution in comparison to the photoresists that include DETC). According to the Gibbs free energies reported in Fig. 6 and Table S24,† the C–H cleavage of PETA with the inter-HAT reaction in the

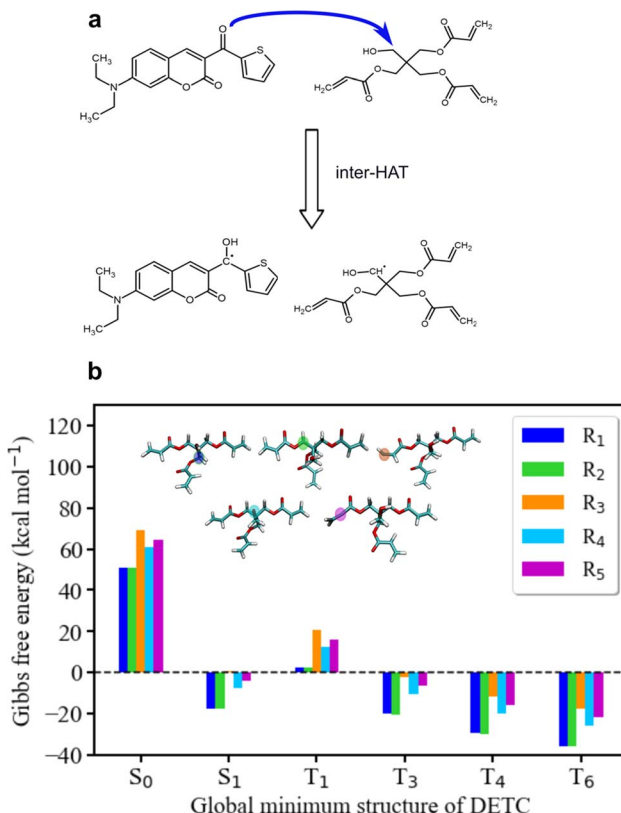


Fig. 6 Radical reaction mechanisms between DETC and PETA. (a) HAT reaction between DETC in a high triplet state and PETA in the ground state that leads to the formation of a ketyl radical on DETC and an alkyl radical on PETA (R<sub>1</sub> or R<sub>2</sub>) that consequently initiates the polymerization (R<sub>1</sub> is reported in the figure). It is important to note that all carbon atoms in the alpha position with respect to the central carbon atom in the pentaerythritol fragment of PETA are equally susceptible to form radicals. (b) Gibbs free energy of the reaction involving different PETA radicals (R<sub>1</sub>–R<sub>5</sub>, see Fig. S18†) as a function of the electronic state of DETC (see Table S24†). Energies were computed employing (U)CAM-B3LYP-D3(BJ)/def2-TZVP approach in implicit ACN.

presence of DETC should be easier permitted if DETC is in, *e.g.*, T<sub>1</sub> state, resulting in the formation of the R<sub>1</sub> or R<sub>2</sub> type PETA radical. However, such a reaction is still not spontaneous.

The formation of radicals with the participation of the T<sub>1</sub> state of DETC (for photoresists without co-initiator) was suggested in several reports.<sup>4,16,17,91</sup> To our knowledge, there is no experimental evidence of such radicals formed or reaction mechanisms reported. Since the Gibbs free energy of a similar HAT reaction between DETC (in T<sub>1</sub>) and DBA is even lower than for the reaction with PETA (0.44 kcal mol<sup>−1</sup> *vs.* 5.47 kcal mol<sup>−1</sup>, see Table S25†) and this reaction could not be observed in the printing conditions (see Fig. 3b) (even if the reaction rate is  $7.33 \times 10^7$  s<sup>−1</sup> as calculated using the activation energy barrier presented in Fig. S19†), we tend to believe that the HAT reaction between PETA and DETC should not occur, when DETC is in T<sub>1</sub> excited state. The Gibbs free energy for this reaction when DETC is in higher triplet states is significantly reduced, *i.e.*, even to −29.47 kcal mol<sup>−1</sup> or to −35.62 kcal mol<sup>−1</sup> for DETC in T<sub>4</sub> and T<sub>6</sub> triplet states, respectively (Fig. 6b and Table S25†). Thus, they

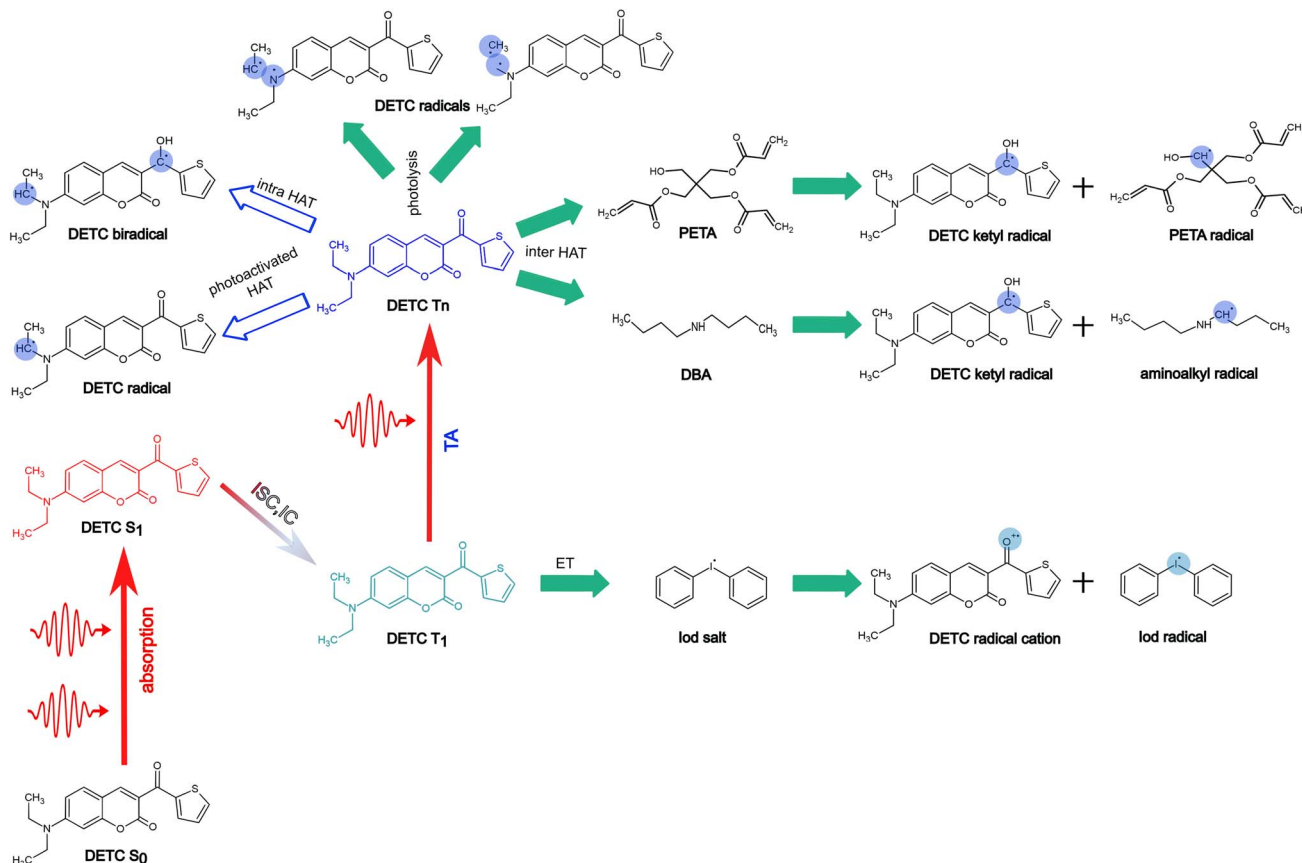


Fig. 7 Summary of radical formation mechanisms during 3D printing in the presence of the DETC photosensitizer considered in the present study. Multiphoton excitation of DETC to the first singlet excited state  $S_1$ , subsequent ISC to triplet  $T_3$  and IC to triplet  $T_1$  followed by TA to higher triplet states are depicted. Radical formation pathways, involving  $T_1$  and  $T_4$  excited states; ET (electron transfer) with onium salt (diphenyliodonium hexafluorophosphate, DPIHFP) involves  $T_1$  of DETC, thus nonlinearity of  $N \sim 2$ , whereas higher triplet state(s) should activate inter-HAT reactions with PETA or DBA co-initiator or photolysis, scaling with  $N \sim 3$ . Formation of aminoalkyl DETC radicals or biradicals via photoactivated HAT is hindered.

are more prone to compete with internal photophysical processes in DETC, suggesting reactions to happen from such states. Due to the convergence problems in optimizing transition states involving PETA and DETC in high triplet states, we cannot provide rates of such reactions, however, the radical formation pathway mentioned helps in rationalizing experimental observations. It should be noted that the calculated rates and Gibbs free energies represent values in equilibrium conditions without population distribution of excited states, various decay pathways, light intensity *etc.* They were aimed to reveal molecular bases of the complex processes during TPP with DETC.

From all reaction pathways examined, we conclude that DETC may be susceptible to radical generation through the inter-HAT involving the PETA monomer or photolysis, which are both spontaneous even in the absence of a co-initiator. Experimental confirmation of an exact radical species by, *e.g.*, the in-depth analysis of the chemical composition of the 3D laser printed materials is still necessary. Since these processes are more spontaneous with the participation of DETC in higher

triplet states, reached upon TA, the third-order dependency and exceptional efficiency of this PI in FRP are experimentally observed.

In Fig. 7, we summarize pathways of the multiphoton activation of DETC in 3D printing with fs lasers of the wavelength of  $\sim 800$  nm, as well as the radical generation mechanisms considered in this work. Pathways, resulting in possibly the most active radical formation, are marked with the filled green arrows, whereas pathways that are hindered due to various reasons, explained in Section 9 in ESI<sup>†</sup> (*i.e.* DETC radicals), are marked with empty blue arrows. Note that different PETA radicals with the activated carbon atoms in the alpha position with respect to the central carbon atom in the pentaerythritol fragment of PETA can occur. The mechanisms of FRP are explained in detail in Section 10 in ESI<sup>†</sup>. More investigation from an experimental point of view is, therefore, necessary to further validate theoretically predicted radical formation mechanisms and the reactivity of DETC in its  $T_1$  state in comparison to the higher triplet states.



## Conclusions

3D laser nanoprinting techniques and photoresist systems have advanced significantly over the past decade. A consensus has emerged that the PI is a key ingredient in the complex interplay of factors that control the speed and resolution of 3D laser nanoprinting. However, the molecular basis of photoactivation during 3D printing is still not well understood. Herein, we have provided an in-depth analysis of the photoactivation and photoreactivity of DETC, one of the most efficient, presently used, multiphoton photoinitiators, to explain the mechanisms of FRP in 3D printing using DETC. We have demonstrated the second-order scaling of the DETC reactivity with DPIHFP onium salt and provided a molecular understanding of the formation of radicals in a two-component bimolecular system comprising DETC and the DBA co-initiator as well as DETC and the PETA monomer.

We have shown that in a one-component system, *i.e.*, in the absence of a co-initiator, the FRP initiation with nonlinearity of 2 is not allowed, since the electronic structure of DETC in the  $T_1$  excited state does not permit active radical formation, which typically occurs for unimolecular processes for Norrish type I PIs. The BDE of C–H, C–C or C–N bond cleavage of DETC, aimed to open the pathway for reactive radicals, is too high in  $T_1$  ( $\sim 22\text{--}51$  kcal mol $^{-1}$ ). However, bond breaking affinity of DETC changes significantly upon TA absorption of the third photon at *ca.* 800 nm. This wavelength fits well to the triplet-triplet transition of DETC from its  $T_1$  to higher triplet states, *e.g.*,  $T_4$ , modulating the electronic structure of DETC towards easier H-atom abstraction reactions or C–C and C–N bond cleavage. However, H-atom abstraction-based hypothetical pathways for the radical creation are not spontaneous and cannot compete with fast internal conversion to  $T_1$ , hindering the formation of active DETC radicals and biradicals during 3D printing that could directly initiate FRP. The Gibbs free energy of photolysis of DETC in high excited states shows higher spontaneity (*i.e.*,  $-0.52$  to  $-26.96$  kcal mol $^{-1}$  from the  $T_4$  excited state), however further experimental validation is required.

We demonstrate that the radicals that could, indeed, initiate FRP (especially in the absence of a co-initiator) are alkyl-based radicals of PETA, formed upon H-atom abstraction reaction between PETA and DETC. The rate of this reaction, from the  $T_1$  excited state of DETC, should be lower than the reaction of DETC with DBA (*i.e.*, the rate of  $7.33 \times 10^7$  s $^{-1}$ ). Since the latter is not observed experimentally, we demonstrate that the formation of reactive radicals occurs in the presence of DETC excited to higher triplet states. In both cases, for PETA and DBA, HAT with DETC in high triplets should be spontaneous. When these reactions are capable of competing with photophysical processes, such as IC and RISC, they will initiate FRP according to mechanisms suggested in this study.

The provided in-depth investigation of DETC photosensitization permits the understanding of the pathways initiating polymerization of photoresist compositions comprising DETC during 3D printing. It addresses ongoing challenges in rapid 3D laser nanoprinting by providing possible ways for more

sensitive PIs, such as enhanced capabilities of HAT abstraction either from a co-initiator or a monomer used in a such photopolymerization.

## Data availability

The raw data of this publication are permanently available on our institutional repository and can be referenced *via* this link <https://www.radar-service.eu/radar/en/dataset/KjeSQpjIkSHeqhFY?token=ZOuvquDpJMfJJufuEfo>.

## Author contributions

A. M.: quantum mechanical calculations, investigation, data analysis and visualization, drafting the paper, paper review and editing; P. K.: nonlinearity measurements, experiment-theory feedback loops and analysis, paper review and editing; P. N.: discussion, data interpretation, paper review and editing; T. M.: nonlinearity measurements, discussion and data interpretation, paper review and editing; N. M. B: discussion, data interpretation, paper review and editing; L. Y.: discussion, data interpretation, paper review and editing; S. W.: discussion, data interpretation, paper review and editing; A. N. U.: discussion, data interpretation, paper review and editing; C. B. K.: discussion, data interpretation, paper review and editing; M. W.: discussion and data interpretation, paper review and editing; W. W.: discussion and data interpretation, funding acquisition, resources, paper review and editing; M. K.: conceptualization, supervision, project administration, investigation, data analysis, funding acquisition, paper writing, review and editing.

## Conflicts of interest

There are no conflicts to declare.

## Acknowledgements

This research has been funded by Deutsche Forschungsgemeinschaft (DFG, German Research Foundation) under Germany's Excellence Strategy for the Excellence Cluster "3D Matter Made to Order" (Grant No. EXC-2082/1-390761711) and by the Carl Zeiss Foundation. C. B. K. acknowledges the Australian Research Council (ARC) for funding in the context of a Laureate Fellowship. M. K. acknowledges funding by the Ministry of Science, Research and Art of Baden-Württemberg (Germany) under Brigitte-Schlieben-Lange-Programm. The authors acknowledge support by the state of Baden-Württemberg through bwHPC and the German Research Foundation (DFG) through grant no INST 40/575-1 FUGG (JUSTUS 2 cluster) under project bw20F004. We acknowledge support by the KIT-Publication Fund of the Karlsruhe Institute of Technology. We acknowledge Guangjun Tian, Yanshan University (China), for providing the Dynavib code and for the assistance in ensuring its proper utilization.



## Notes and references

1 C. Barner-Kowollik, M. Bastmeyer, E. Blasco, G. Delaittre, P. Müller, B. Richter, *et al.*, 3D Laser Micro- and Nanoprinting: Challenges for Chemistry, *Angew. Chem., Int. Ed.*, 2017, **56**(50), 15828–15845.

2 J. Fischer, J. B. Mueller, J. Kaschke, T. J. A. Wolf, A. N. Unterreiner and M. Wegener, Three-dimensional multi-photon direct laser writing with variable repetition rate, *Opt. Express*, 2013, **21**(22), 26244–26260.

3 X. He, T. Li, J. Zhang and Z. Wang, STED Direct Laser Writing of 45 nm Width Nanowire, *Micromachines*, 2019, **10**(11), 726.

4 J. Fischer, J. B. Mueller, A. S. Quick, J. Kaschke, C. Barner-Kowollik and M. Wegener, Exploring the Mechanisms in STED-Enhanced Direct Laser Writing, *Adv. Opt. Mater.*, 2015, **3**(2), 221–232.

5 J. Fischer and M. Wegener, Three-dimensional optical laser lithography beyond the diffraction limit, *Laser Photonics Rev.*, 2013, **7**(1), 22–44.

6 E. Sedghamiz, M. Liu and W. Wenzel, Challenges and limits of Mechanical Stability in 3D Direct Laser Writing, *Nat. Commun.*, 2022, **13**, 2115.

7 Z. Bai, J. Wei, X. Liang, K. Zhang, T. Wei and R. Wang, High-speed laser writing of arbitrary patterns in polar coordinate system, *Rev. Sci. Instrum.*, 2016, **87**(12), 125118.

8 H. Yuk, B. Lu, S. Lin, K. Qu, J. Xu, J. Luo, *et al.*, 3D printing of conducting polymers, *Nat. Commun.*, 2020, **11**(1), 1604.

9 M. Hippler, E. D. Lemma, S. Bertels, E. Blasco, C. Barner-Kowollik, M. Wegener, *et al.*, 3D Scaffolds to Study Basic Cell Biology, *Adv. Mater.*, 2019, **31**(26), 1808110.

10 S. J. Zhang, Y. Li, Y. K. Wang, L. P. Liu, H. D. Wang, Y. F. Xiao, *et al.*, Controlling Young's modulus of polymerized structures fabricated by direct laser writing, *Appl. Phys. A*, 2015, **118**(2), 437–441.

11 P. Kiefer, V. Hahn, M. Nardi, L. Yang, E. Blasco, C. Barner-Kowollik, *et al.*, Sensitive Photoresists for Rapid Multiphoton 3D Laser Micro- and Nanoprinting, *Adv. Opt. Mater.*, 2020, **8**(19), 2000895.

12 T. Chi, P. Somers, D. A. Wilcox, A. J. Schuman, V. Iyer, R. Le, *et al.*, Tailored thioxanthone-based photoinitiators for two-photon-controllable polymerization and nanolithographic printing, *J. Polym. Sci., Part B: Polym. Phys.*, 2019, **57**(21), 1462–1475.

13 B. Holzer, M. Lunzer, A. Rosspeintner, G. Licari, M. Tromayer, S. Naumov, *et al.*, Towards efficient initiators for two-photon induced polymerization: fine tuning of the donor/acceptor properties, *Mol. Syst. Des. Eng.*, 2019, **4**(2), 437–448.

14 P. Hu, W. Qiu, S. Naumov, T. Scherzer, Z. Hu, Q. Chen, *et al.*, Conjugated Bifunctional Carbazole-Based Oxime Esters: Efficient and Versatile Photoinitiators for 3D Printing under One- and Two-Photon Excitation, *ChemPhotoChem*, 2020, **4**(3), 224–232.

15 M. Tromayer, P. Gruber, A. Rosspeintner, A. Ajami, W. Husinsky, F. Plasser, *et al.*, Wavelength-optimized Two-Photon Polymerization Using Initiators Based on Multipolar Aminostyryl-1,3,5-triazines, *Sci. Rep.*, 2018, **8**(1), 17273.

16 J. Tang, X. Xu, X. Shen, C. Kuang, H. Chen, M. Shi, *et al.*, Ketocoumarin-Based Photoinitiators for High-Sensitivity Two-Photon Lithography, *ACS Appl. Polym. Mater.*, 2023, **5**(4), 2956–2963.

17 P. Somers, Z. Liang, T. Chi, J. E. Johnson, L. Pan, B. W. Boudouris, *et al.*, Photo-activated polymerization inhibition process in photoinitiator systems for high-throughput 3D nanoprinting, *Nanophotonics*, 2023, **12**, 1571–1580.

18 N. Liaros, S. A. Gutierrez Razo, M. D. Thum, H. M. Ogden, A. N. Zeppuhar, S. Wolf, *et al.*, Elucidating complex triplet-state dynamics in the model system isopropylthioxanthone, *iScienc*, 2022, **25**(1), 103600.

19 S. Dadashi-Silab, S. Doran and Y. Yagci, Photoinduced Electron Transfer Reactions for Macromolecular Syntheses, *Chem. Rev.*, 2016, **116**(17), 10212–10275.

20 C. S. Colley, D. C. Grills, N. A. Besley, S. Jockusch, P. Matousek, A. W. Parker, *et al.*, Probing the Reactivity of Photoinitiators for Free Radical Polymerization: Time-Resolved Infrared Spectroscopic Study of Benzoyl Radicals, *J. Am. Chem. Soc.*, 2002, **124**(50), 14952–14958.

21 Y. Yagci, S. Jockusch and N. J. Turro, Photoinitiated Polymerization: Advances, Challenges, and Opportunities, *Macromolecules*, 2010, **43**(15), 6245–6260.

22 B. Jana, S. R. Inamdar and H. M. Suresh Kumar, Effect of quencher and temperature on fluorescence intensity of laser dyes: DETC and C504T, *Spectrochim. Acta, Part A*, 2017, **170**, 124–130.

23 J. L. R. Williams, D. P. Specht and S. Farid, Ketocoumarins as photosensitizers and photoinitiators, *Polym. Eng. Sci.*, 1983, **23**(18), 1022–1024.

24 S. Sarkar, K. P. S. Cheung and V. Gevorgyan, C–H functionalization reactions enabled by hydrogen atom transfer to carbon-centered radicals, *Chem. Sci.*, 2020, **11**(48), 12974–12993.

25 J. Xie, P. Xu, Y. Zhu, J. Wang, W. C. C. Lee and X. P. Zhang, New Catalytic Radical Process Involving 1,4-Hydrogen Atom Abstraction: Asymmetric Construction of Cyclobutanones, *J. Am. Chem. Soc.*, 2021, **143**(30), 11670–11678.

26 J. P. Fouassier, D. Ruhlmann, B. Graff, F. Morlet-Savary and F. Wieder, Excited state processes in polymerization photoinitiators, *Prog. Org. Coat.*, 1995, **25**(3), 235–271.

27 J. Kabatc, J. Ortyl and K. Kostrzewska, New kinetic and mechanistic aspects of photosensitization of iodonium salts in photopolymerization of acrylates, *RSC Adv.*, 2017, **7**(66), 41619–41629.

28 K. J. Schafer, J. M. Hales, M. Balu, K. D. Belfield, E. W. Van Stryland and D. J. Hagan, Two-photon absorption cross-sections of common photoinitiators, *J. Polym. Sci., Part A: Polym. Chem.*, 2004, **42**(2–3), 497–502.

29 L. Yang, A. Münchinger, M. Kadic, V. Hahn, F. Mayer, E. Blasco, *et al.*, On the Schwarzschild Effect in 3D Two-Photon Laser Lithography, *Adv. Opt. Mater.*, 2019, **7**(22), 1901040.



30 J. Fischer and M. Wegener, Three-dimensional direct laser writing inspired by stimulated-emission-depletion microscopy [Invited], *Opt. Mater. Express*, 2011, **1**(4), 614–624.

31 B. Harke, W. Dallari, G. Grancini, D. Fazzi, F. Brandi, A. Petrozza, *et al.*, Polymerization Inhibition by Triplet State Absorption for Nanoscale Lithography, *Adv. Mater.*, 2013, **25**(6), 904–909.

32 T. Yanai, D. P. Tew and N. C. Handy, A new hybrid exchange–correlation functional using the Coulomb-attenuating method (CAM-B3LYP), *Chem. Phys. Lett.*, 2004, **393**(1–3), 51–57.

33 A. Schäfer, H. Horn and R. Ahlrichs, Fully optimized contracted Gaussian basis sets for atoms Li to Kr, *J. Chem. Phys.*, 1992, **97**(4), 2571–2577.

34 S. Grimme, S. Ehrlich and L. Goerigk, Effect of the damping function in dispersion corrected density functional theory, *J. Comput. Chem.*, 2011, **32**(7), 1456–1465.

35 M. J. Frisch, G. W. Trucks, H. B. Schlegel, G. E. Scuseria, M. A. Robb, J. R. Cheeseman, *et al.*, *Gaussian 16*, Gaussian, Inc., Wallingford, CT, 2016.

36 G. Scalmani and M. J. Frisch, Continuous surface charge polarizable continuum models of solvation. I. General formalism, *J. Chem. Phys.*, 2010, **132**(11), 114110.

37 F. J. Avila Ferrer, J. Cerezo, E. Stendardo, R. Improta and F. Santoro, Insights for an Accurate Comparison of Computational Data to Experimental Absorption and Emission Spectra: Beyond the Vertical Transition Approximation, *J. Chem. Theory Comput.*, 2013, **9**(4), 2072–2082.

38 D. Jacquemin, A. Planchat, C. Adamo and B. Mennucci, TD-DFT Assessment of Functionals for Optical 0–0 Transitions in Solvated Dyes, *J. Chem. Theory Comput.*, 2012, **8**(7), 2359–2372.

39 K. Krause and W. Klopper, Implementation of the Bethe–Salpeter equation in the TURBOMOLE program, *J. Comput. Chem.*, 2017, **38**(6), 383–388.

40 M. J. van Setten, F. Weigend and F. Evers, The GW -Method for Quantum Chemistry Applications: Theory and Implementation, *J. Chem. Theory Comput.*, 2013, **9**(1), 232–246.

41 TURBOMOLE V7.4 2019, A development of University of Karlsruhe and Forschungszentrum Karlsruhe GmbH, 1989–2007, TURBOMOLE GmbH, since 2007, available from <https://www.turbomole.org/>.

42 T. Lu and F. Chen, Multiwfn: A multifunctional wavefunction analyzer, *J. Comput. Chem.*, 2012, **33**(5), 580–592.

43 G. Temel, D. S. Esen and N. Arsu, One-component benzoxazine type photoinitiator for free radical polymerization, *Polym. Eng. Sci.*, 2012, **52**(1), 133–138.

44 Z. Shuai and Q. Peng, Organic light-emitting diodes: theoretical understanding of highly efficient materials and development of computational methodology, *Natl. Sci. Rev.*, 2017, **4**(2), 224–239.

45 Y. Niu, W. Li, Q. Peng, H. Geng, Y. Yi, L. Wang, *et al.*, MOlecular MAterials Property Prediction Package (MOMAP) 1.0: a software package for predicting the luminescent properties and mobility of organic functional materials, *Mol. Phys.*, 2018, **116**(7–8), 1078–1090.

46 Q. Peng, Y. Yi, Z. Shuai and J. Shao, Excited state radiationless decay process with Duschinsky rotation effect: Formalism and implementation, *J. Chem. Phys.*, 2007, **126**(11), 114302.

47 Q. Peng, Y. Niu, Q. Shi, X. Gao and Z. Shuai, Correlation Function Formalism for Triplet Excited State Decay: Combined Spin–Orbit and Nonadiabatic Couplings, *J. Chem. Theory Comput.*, 2013, **9**(2), 1132–1143.

48 Y. Niu, Q. Peng and Z. Shuai, Promoting-mode free formalism for excited state radiationless decay process with Duschinsky rotation effect, *Sci. China, Ser. B: Chem.*, 2008, **51**(12), 1153–1158.

49 Y. Niu, Q. Peng, C. Deng, X. Gao and Z. Shuai, Theory of Excited State Decays and Optical Spectra: Application to Polyatomic Molecules, *J. Phys. Chem. A*, 2010, **114**(30), 7817–7831.

50 P. Jørgensen, H. J. A. Jensen and J. Olsen, Linear response calculations for large scale multiconfiguration self-consistent field wave functions, *J. Chem. Phys.*, 1988, **89**(6), 3654–3661.

51 M. T. P. Beerepoot, D. H. Friese, N. H. List, J. Kongsted and K. Ruud, Benchmarking two-photon absorption cross sections: performance of CC2 and CAM-B3LYP, *Phys. Chem. Chem. Phys.*, 2015, **17**(29), 19306–19314.

52 C. Hättig, O. Christiansen and P. Jørgensen, Multiphoton transition moments and absorption cross sections in coupled cluster response theory employing variational transition moment functionals, *J. Chem. Phys.*, 1998, **108**(20), 8331–8354.

53 P. Cronstrand, P. Norman, Y. Luo and H. Ågren, Few-states models for three-photon absorption, *J. Chem. Phys.*, 2004, **121**(5), 2020–2029.

54 K. Aidas, C. Angeli, K. L. Bak, V. Bakken, R. Bast, L. Boman, *et al.*, The Dalton quantum chemistry program system: The Dalton program, *Wiley Interdiscip. Rev.: Comput. Mol. Sci.*, 2014, **4**(3), 269–284.

55 F. Santoro, A. Lami, R. Improta, J. Bloino and V. Barone, Effective method for the computation of optical spectra of large molecules at finite temperature including the Duschinsky and Herzberg–Teller effect: The Qx band of porphyrin as a case study, *J. Chem. Phys.*, 2008, **128**(22), 224311.

56 G. Herzberg and E. Teller, Schwingungsstruktur der Elektronenübergänge bei mehratomigen Molekülen, *Z. Phys. Chem.*, 1933, **21B**(1), 410–446.

57 G. Tian, S. Duan, W. Hua, and Y. Luo, *DynaVib Version 1.0*, R Inst Technol Swed, 2012.

58 Y. Pan, L. Li, F. Qiu, Y. Wei, W. Hua and G. Tian, On the spectral profile change in the Q band absorption spectra of metalloporphyrins (Mg, Zn, and Pd): A first-principles study, *J. Chem. Phys.*, 2019, **150**(16), 164308.



59 E. v. Lenthe, E. J. Baerends and J. G. Snijders, Relativistic regular two-component Hamiltonians, *J. Chem. Phys.*, 1993, **99**(6), 4597–4610.

60 G. Tian and Y. Luo, Isomer-Dependent Franck–Condon Blockade in Weakly Coupled Bipyridine Molecular Junctions, *J. Phys. Chem. C*, 2014, **118**(27), 14853–14859.

61 G. Tian and Y. Luo, Fluorescence and Phosphorescence of Single C<sub>60</sub> Molecules as Stimulated by a Scanning Tunneling Microscope, *Angew. Chem., Int. Ed.*, 2013, **52**(18), 4814–4817.

62 M. Caricato, B. Mennucci, J. Tomasi, F. Ingrosso, R. Cammi, S. Corni, *et al.*, Formation and relaxation of excited states in solution: A new time dependent polarizable continuum model based on time dependent density functional theory, *J. Chem. Phys.*, 2006, **124**(12), 124520.

63 R. Improta, G. Scalmani, M. J. Frisch and V. Barone, Toward effective and reliable fluorescence energies in solution by a new state specific polarizable continuum model time dependent density functional theory approach, *J. Chem. Phys.*, 2007, **127**(7), 074504.

64 R. Improta, V. Barone, G. Scalmani and M. J. Frisch, A state-specific polarizable continuum model time dependent density functional theory method for excited state calculations in solution, *J. Chem. Phys.*, 2006, **125**(5), 054103.

65 S. Wu, L. A. Galán, M. Roux, F. Riobé, B. Le Guennic, Y. Guyot, *et al.*, Tuning Excited-State Properties of [2.2] Paracyclophane-Based Antennas to Ensure Efficient Sensitization of Lanthanide Ions or Singlet Oxygen Generation, *Inorg. Chem.*, 2021, **60**(21), 16194–16203.

66 Y. Zhang, Y. Su, Y. Zhao, Z. Wang and C. Wang, Two-Photon 3D Printing in Metal–Organic Framework Single Crystals, *Small*, 2022, **18**(18), 2200514.

67 S. De Regardati, J. Pahapill, A. Mikhailov, Y. Stepanenko and A. Rebane, High-accuracy reference standards for two-photon absorption in the 680–1050 nm wavelength range, *Opt. Express*, 2016, **24**(8), 9053.

68 N. S. Makarov, M. Drobizhev and A. Rebane, Two-photon absorption standards in the 550–1600 nm excitation wavelength range, *Opt. Express*, 2008, **16**(6), 4029.

69 C. A. Farfan and D. B. Turner, A systematic model study quantifying how conical intersection topography modulates photochemical reactions, *Phys. Chem. Chem. Phys.*, 2020, **22**(36), 20265–20283.

70 I. Cohanoschi, K. D. Belfield and F. E. Hernández, Three-photon absorption enhancement in symmetrical charge transfer pull-pull fluorene derivatives, *Chem. Phys. Lett.*, 2005, **406**(4–6), 462–466.

71 M. P. Shortell, E. A. Jaatinen, J. Chang and E. R. Waclawik, Using pulse transit delay in Z-scan to discriminate between excited-state absorption and other nonlinear processes in ZnO nanocones, *Opt. Express*, 2014, **22**(6), 6222.

72 J. Lalevée, X. Allonas and J. P. Fouassier, N–H and  $\alpha$ (C–H) Bond Dissociation Enthalpies of Aliphatic Amines, *J. Am. Chem. Soc.*, 2002, **124**(32), 9613–9621.

73 M. Abdallah, F. Dumur, A. Hijazi, G. Rodeghiero, A. Gualandi, P. G. Cozzi, *et al.*, Keto-coumarin scaffold for photoinitiators for 3D printing and photocomposites, *J. Polym. Sci.*, 2020, **58**(8), 1115–1129.

74 M. Abdallah, A. Hijazi, B. Graff, J. P. Fouassier, G. Rodeghiero, A. Gualandi, *et al.*, Coumarin derivatives as versatile photoinitiators for 3D printing, polymerization in water and photocomposite synthesis, *Polym. Chem.*, 2019, **10**(7), 872–884.

75 G. L. Thornton, R. Phelps and A. J. Orr-Ewing, Transient absorption spectroscopy of the electron transfer step in the photochemically activated polymerizations of N-ethylcarbazole and 9-phenylcarbazole, *Phys. Chem. Chem. Phys.*, 2021, **23**(34), 18378–18392.

76 D. S. Achilias, A Review of Modeling of Diffusion Controlled Polymerization Reactions, *Macromol. Theory Simul.*, 2007, **16**(4), 319–347.

77 L. Ravotto, S. L. Meloni, T. V. Esipova, A. E. Masunov, J. M. Anna and S. A. Vinogradov, Three-Photon Spectroscopy of Porphyrins, *J. Phys. Chem. A*, 2020, **124**(52), 11038–11050.

78 H. Eyring, The Activated Complex in Chemical Reactions, *J. Chem. Phys.*, 1935, **3**(2), 107–115.

79 T. Xue, Y. Li, X. Li, B. Huang, Q. Song, J. Nie, *et al.*, Benzylidene ketones as visible light radical photoinitiator: The effects of electron-donating group and co-initiator, *J. Polym. Sci., Part A: Polym. Chem.*, 2021, **418**, 113395.

80 P. Wiggins, J. A. G. Williams and D. J. Tozer, Excited state surfaces in density functional theory: A new twist on an old problem, *J. Chem. Phys.*, 2009, **131**(9), 091101.

81 C. M. Marian, Spin–orbit coupling and intersystem crossing in molecules: Spin–orbit coupling, *Wiley Interdiscip. Rev.: Comput. Mol. Sci.*, 2012, **2**(2), 187–203.

82 V. Balzani, P. Ceroni, and A. Juris, *Photochemistry and photophysics: concepts, research, applications*, Wiley-VCH, Weinheim, 2014, p. 472.

83 S. K. Lower and M. A. El-Sayed, The Triplet State and Molecular Electronic Processes in Organic Molecules, *Chem. Rev.*, 1966, **66**(2), 199–241.

84 T. J. Penfold, E. Gindensperger, C. Daniel and C. M. Marian, Spin–Vibronic Mechanism for Intersystem Crossing, *Chem. Rev.*, 2018, **118**(15), 6975–7025.

85 L. Capaldo, D. Ravelli and M. Fagnoni, Direct Photocatalyzed Hydrogen Atom Transfer (HAT) for Aliphatic C–H Bonds Elaboration, *Chem. Rev.*, 2022, **122**(2), 1875–1924.

86 S. K. Dogruyol, Z. Dogruyol and N. Arsu, A thioxanthone-based visible photoinitiator: Thioxanthone-based Visible Photoinitiator, *J. Polym. Sci., Part A: Polym. Chem.*, 2011, **49**(18), 4037–4043.

87 G. Temel, B. Enginol, M. Aydin, D. K. Balta and N. Arsu, Photopolymerization and photophysical properties of amine linked benzophenone photoinitiator for free radical polymerization, *J. Polym. Sci., Part A: Polym. Chem.*, 2011, **219**(1), 26–31.

88 G. Ding, C. Jing, X. Qin, Y. Gong, X. Zhang, S. Zhang, *et al.*, Conjugated dyes carrying N, N-dialkylamino and ketone groups: One-component visible light Norrish type II photoinitiators, *Dyes Pigm.*, 2017, **137**, 456–467.



89 J. P. Fouassier, D. Ruhlmann, Y. Takimoto, M. Harada and M. Kawabata, New three-component initiation systems in UV curing: A time-resolved laser-spectroscopy investigation, *J. Polym. Sci., Part A: Polym. Chem.*, 1993, **31**(9), 2245–2248.

90 X. Pan, M. A. Tasdelen, J. Laun, T. Junkers, Y. Yagci and K. Matyjaszewski, Photomediated controlled radical polymerization, *Prog. Polym. Sci.*, 2016, **62**, 73–125.

91 J. E. Johnson, Y. Chen and X. Xu, Model for polymerization and self-deactivation in two-photon nanolithography, *Opt. Express*, 2022, **30**(15), 26824.

